Mechanical gating of the auditory transduction channel TMC1 involves the fourth and sixth transmembrane helices

Nurunisa Akyuz[1*], K. Domenica Karavitaki[1*], Bifeng Pan[1*], Panos I. Tamvakologos[1], Kelly P. Brock[2], Yaqiao Li[1], Debora S. Marks[2], David P. Corey[1]

[1]Department of Neurobiology and [2]Department of Systems Biology, Harvard Medical School, Boston, MA 02115, USA

*Equal contributions (listed alphabetically)

Abstract:

The transmembrane channel-like (TMC) 1 and 2 proteins play a central role in auditory transduction, forming ion channels that convert sound into electrical signals. However, the molecular mechanism of their gating remains unknown. Here, using predicted structural models as a guide, we probed the effects of twelve mutations on the mechanical gating of the transduction currents in native hair cells of *Tmc1/2*-null mice expressing virally introduced TMC1 variants. Whole-cell electrophysiological recordings revealed that mutations within the pore-lining transmembrane (TM) helices 4 and 6 modified gating, reducing the force sensitivity or shifting the open probability of the channels, or both. For some of the mutants, these changes were accompanied by a change in single-channel conductance. Our observations are in line with a model wherein conformational changes in the TM4 and TM6 helices are involved in the mechanical gating of the transduction channel.

1   Introduction

2   Our sense of hearing relies on the conversion of sound-induced mechanical stimuli into neural
3   signals by cochlear hair cells of the inner ear. This process hinges on the ability of sensory
4   transduction channels in hair cells to respond to mechanical stimuli by opening and closing,
5   thereby generating fluctuating receptor currents[1]. Despite decades of research, it was difficult to
6   determine the molecular identity of the transduction channel. A number of proteins including
7   transmembrane channel-like 1 and 2 (TMC1 and TMC2), lipoma HMGIC fusion partner-like 5
8   (LHFPL5), transmembrane inner ear expressed protein (TMIE) and calcium and integrin binding
9   protein (CIB2) are now known to be essential for mechanotransduction [2, 3, 4, 5] but their specific
10   roles were not clear.

11   TMCs can assemble as dimers in solution and are structurally related to the TMEM16 and
12   TMEM63/OSCA proteins[6, 7, 8]. Each subunit of the dimer is thought to contain ten transmembrane
13   (TM) helices (**Supplementary Fig. 1A-B**). Parts of the N-terminus (residues 100-130 in mouse
14   TMC1) as well as the intracellular loop between TM helices 2-3 (residues 300-350) have been
15   implicated in binding to the auxiliary channel subunit CIB2 [3, 9]. Currently, we do not know the
16   mode of dimerization; however the models based on X-ray and cryo-EM structures of TMEM16
17   proteins[6, 8] suggest that the subunit interface is near TM10 and may be at least partly filled with
18   lipid as has been observed in TMEM16 and OSCA protein families (**Supplementary Fig. 1B**)[10] or
19   perhaps by auxiliary proteins[11].

20   Experiments with spontaneous and engineered mutations of the TMC1 protein have now
21   indicated that TMC1 (and likely TMC2) is a pore-forming protein of the mechanotransduction
22   complex[5, 6]. Each subunit of the dimer includes a separate ion-conducting pore, which is a large
23   open cavity that is surrounded by TM helices 4-7 (**Supplementary Fig. 1B**) [6, 8, 12]. Channel activity
24   of TMC homologs expressed in heterologous cell lines[13] is also consistent with the idea that TMC1
25   and TMC2 constitute most or all of the transduction channel pore.

26   These experiments did not, however, shed light on gating—on the mechanically evoked
27   conformational changes that open and close the pore. Conformational states associated with
28   conduction have been suggested for the related ion channels and lipid scramblases of the
29   TMEM16 family.   Specifically, in TMEM16 chloride channels and lipid scramblases, Ca^{2+}-
30   activated opening is thought to involve an initial rearrangement of the 'gating helix' TM6[14, 15].
31   Channel opening further requires disruption of interactions between TM4 and TM6[16, 17].

32   Molecular dynamic simulations of TMC1 structural models based on TMEM16 proteins suggest
33   that the TMC1 pore can adopt two distinct conformations. In one conformation, TM4 are about
34   4 Å further from TM6 than in the other, and in simulations of K^+ ion passage through the pore,
35   the more open conformation conducted ions about three times faster[12]. These studies provide
36   starting points for probing the gating of TMC1 physiologically.

37   In this study, for the first time, we probe the relationship between the structure of TMC1 and the
38   mechanical activation of the hair-cell transduction channel. We used structure-prediction

39 algorithms to further explore potential conformations of TMC1. Based on these, we designed
40 mutations in TM4 and TM6 that might affect gating. We used AAV vectors to express, in hair
41 cells of *Tmc1/2* double-knockout (DKO) mice, TMC1 channels bearing specific mutations and we
42 recorded mechanotransduction currents from cochlear hair cells. We examined the effects of a
43 dozen mutations on mechanical gating of the transduction currents in mouse hair cells in vivo
44 (**Supplementary Table 1).** Shifts in the mechanical activation curves suggested that many of these
45 mutations changed the relative energy of the open state. Furthermore, some of the mutations
46 reduced the slope of the activation curve, suggesting that these mutations render the channel less
47 sensitive to mechanical stimulus. In some cases, these gating changes were accompanied by a
48 decrease in single-channel conductance, measured with nonstationary noise analysis, consistent
49 with TM4 and TM6 also contributing to the permeation pathway[6]. Together, these observations
50 provide evidence for a model of transduction wherein conformational changes involving TM4
51 and TM6 of TMC1 are critical for channel opening induced by hair bundle deflection.

52 Results

53 *Predicted TMC1 Structures*

54 To identify residues that may influence gating, we began with our previous homology model for
55 TMC1[6]. We then generated more refined models using the deep learning-based modeling
56 algorithms, transform-restrained (tr) Rosetta[18] and RoseTTAFold [19] (see Methods, **Fig. 1A**). These
57 methods rely on patterns in protein sequences as well as on amino-acid interactions suggested by
58 co-evolution, and utilize energy minimization techniques[20] to predict protein structures. Without
59 relying on structures of related proteins, both trRosetta and RoseTTAFold predict an overall
60 'TMEM16-like' fold for TMC1 that is very similar to that previously predicted from homology to
61 TMEM16s[6] (**Fig. 1A**).

62 We then performed predictions of the TMC1 structure using the AlphaFold2 program developed
63 by DeepMind[21, 22] (**Fig. 1B**). The predictions with or without utilizing a structural template were
64 nearly identical and were very similar to previous models, especially in regard to the overall fold
65 of the pore region (**Fig. 1B**).

66 These models converge on a pore region in each subunit of the dimer that is formed by TM4-7
67 and exhibits an overall negative electrostatic potential, which is consistent with the cation
68 selectivity of the channel[23, 24, 25]. Several conserved residues within TM6-7 of mTMC1 contribute
69 to this negative surface charge, including E514, E520, D528, D540, D557, E559, D569, E567.
70 Mutations of some of these residues, including D528 and D569, have been linked to hearing loss
71 [26, 27].

72 Running the AlphaFold2 network multiple times using different seeds, we were able to increase
73 the diversity of the predicted structural states (**Fig. 1C**). We generated 20 models (4 random seeds
74 and 5 models from each), and then aligned and clustered these structures using Chimera[2]. By
75 calculating the root-mean-square deviation (RMSD) values for every pair-wise comparison
76 between the 20 models, we found the structures clustered into two groups (16 structures in one

77 group and 4 in the other). In the first group, TM3 and TM4 were close to TM6 ('closed-like'; **Fig.**
78 **1D**). In the second, TM3 and TM4 maintained a close association with each other but were further
79 from TM6 ('open-like'). The distance between the C-α atoms of residues 409 (on TM4) and 531
80 (on TM6) within the pore region is larger by ~5 Å in the open-like structures**.** The HOLE software[28]
81 consistently showed a water-filled pore conformation with a large conduction pathway for the
82 open-like but not closed-like predicted structures (**Supplementary Fig. 2A**). The narrowest part
83 of the pathway in this model occurs where N404 in TM4 approaches the positively charged R523
84 and the hydrophobic L524 in TM6. A thin cross-section of the protein parallel to the membrane
85 near N404 and L524 displays the opening clearly (**Supplementary Fig. 2B**). Notably, the change
86 between the predicted states seems to be driven primarily by a ~10° tilting and translation of TM4
87 together with TM3, but also by smaller movements in TM6 (**Fig. 1D**). Interestingly, even the open-
88 like structures displayed a pore diameter of ~ 6Å in the narrowest dimension, which is smaller
89 than that estimated for this channel based on the sizes of the permeating molecules [8, 29].

90 We then generated 160 structures (32 random but distinct seeds and 5 models each) and mapped
91 residue-residue (R-R) distances to compare the AlphaFold2 generated structures[30]. These maps
92 showed that across the 160 structures there was a large variability in the position of the TM3-5
93 helices with respect to the rest of the protein (TMs 1,2,6-9; **Fig. 1E**). Most of the intracellular TM2-
94 TM3 loop shows variability with the rest of the protein, as does the first half of the TM5-6
95 extracellular loop. However, these two loops also show variability with TM3-5. If the differences
96 between the open-like and closed-like structures predicted by AlphaFold2 in fact represent a
97 gating transition, there may be three distinct domain movements associated with gating.

98 We also generated contact maps by EVcouplings software[31] (see Methods) and mapped them onto
99 the open-like and closed-like structure predictions. Evolutionarily coupled residue pairs (ECs)
100 are found in close proximity in the models, as expected (**Supplementary Fig. 2C**). However, there
101 are notably more contacts (not just ECs) in the closed-like state (**Supplementary Fig. 2C**).

102 Overall, the models generated by AlphaFold2 lead us to hypothesize that in TMC1, as in the
103 structurally similar proteins of the TMEM16 and TMEM63/OSCA families, the pore helices TM4
104 and TM6 separate during gating[15, 32, 33].

105 *Activation curves of virally expressed TMC1 in cochlear hair cells of Tmc1/2-DKO animals*

106 If the pore helices TM4 and TM6 undergo a global rearrangement during gating, then mutations
107 of critical residues within these helices may change the activation of the channel. We therefore
108 designed and assessed the effects of mutations in this region of TMC1 (**Fig. 2A-B, Supplementary**
109 **Table 1**). We generated AAV9-PHP.B viral vectors carrying a sequence encoding either wild-type
110 (WT) or mutated TMC1 (**Fig. 2C**). Viral vectors were individually injected into the inner ears of
111 *Tmc1/2*-DKO animals at postnatal day (P)1, using the round window approach (see Methods; **Fig.**
112 **2C**). Cochlear dissections were performed at P4–P6. The tissue was placed in culture for an
113 additional 3–7 days (**Fig. 2C**, bottom panel). The mid-basal section was used for electrophysiology
114 and the mid-apical section was used to assess viral transduction efficiency and functional rescue
115 using an FM1-43 dye loading assay (see Methods). At this stage of cochlear development, *Tmc2*

116   is mostly down-regulated, but we used *Tmc1/2*-DKO animals to avoid the possibility of any
117   contribution of TMC2 to transduction currents.

118   Consistent with previous findings, we observed that cochlear hair cells of *Tmc1/2*-DKO mice do
119   not take up FM1-43, indicating that they lack functional transduction channels [34, 35]. In contrast,
120   *Tmc1/2*-DKO hair cells transduced with AAV9-PHP.B-*Tmc1* encoding WT-TMC1 showed FM1-
121   43 uptake, indicating rescue of transduction activity (**Fig. 2D**). Specifically, the FM1-43 assay
122   indicated that ~ 90% of inner hair cells (IHCs) expressed functional TMC1 channels. This is in line
123   with recent studies demonstrating the use of AAV9-PHP.B vectors with CMV promoters as
124   highly efficient for driving expression in hair cells [36, 37].

125   Following FM1-43 screening, electrophysiological recordings were performed using a stiff glass
126   probe to stimulate hair bundles and whole-cell patch clamping to record currents, as previously
127   described [6]. First, we recorded currents from IHCs of wild-type mice at P8-P13. Maximum current
128   amplitudes of 660±80 pA (n=4) were obtained. In contrast, DKO hair cells expressing virally
129   expressed WT TMC1 channels yielded receptor currents with maximal amplitudes of 202±33 pA,
130   n=7 (**Fig. 2E**). The amplitude and variability in the whole cell currents were consistent with
131   previous reports [6, 36].

132   To obtain activation curves for TMC1 channels, we measured IHC currents evoked by a series of
133   15 bundle step deflections ranging from -175 to 1050 nm (see Methods). Since the shape and slope
134   of the activation curves reflect properties of individual channels, we normalized the currents for
135   each cell to allow for comparison to other cells (**Fig. 2F**).

136   We fitted the normalized activation curves of the channels with a Boltzmann equation:

137
$$P_0 = \frac{1}{1 + \exp\left[-Z \times \frac{(X - X_0)}{k_B T}\right]}$$

138   Here, Z represents the apparent mechanical sensitivity of the channel; it determines the slope of
139   the activation curve [38]. X_0 represents the bundle deflection at which the channel open probability
140   is 0.5. $k_B T$ is thermal energy (4.1 pN nm at room temperature). The normalized activation curves
141   that we obtained from IHCs of TMC1-injected *Tmc1/2*-DKO mice were consistent with previous
142   observations using the same stimulation technique [5, 6] (**Fig. 2F**). The fits of the activation curves
143   of virally transduced WT-TMC1 in IHCs of *Tmc1/2*-DKO animals yielded Z values of 0.027 ± 0.003
144   pN and X_0 values of 380± 32 nm.

145   Using nonstationary noise analysis of whole cell currents[39, 40] we estimated single channel currents
146   as 12.5 ± 2.5 pA (**Fig. 2G**), which are also in line with our previous measurements [6].

147   *Mutation of a glycine residue on TM4 alters the activation curve*

148   We first targeted glycines within TM4 and TM6 because glycines within transmembrane alpha
149   helices of ion channels tend to act as hinge points for a gating conformational change [41]. There is

150   one glycine within TM4 (G411)[26] which is highly conserved across TMCs (**Fig. 2B, Fig. 3A**);
151   mutations of this residue have been associated with deafness. We mutated this residue to a helix-
152   stabilizing alanine[42] to assess whether reducing the conformational flexibility of TM4 would affect
153   gating.

154   Recordings from IHCs expressing TMC1 channels bearing the G411A mutation yielded
155   maximum currents of 291 ± 38 pA (n=8), which are comparable to those obtained from WT-TMC1
156   injected IHCs (**Fig. 3B).** However, the activation curves of TMC1-G411A were shifted rightward
157   (X_0 = 507 ± 28 nm) compared to WT-TMC1 (X_0=380 ± 32 nm) (**Fig. 3C**). The slopes of the curves,
158   represented by the Z values, were also significantly decreased—from to 0.027 to 0.017 pN. Both
159   these changes were significant with p-values <0.05 (**Fig. 3D**). The single channel current estimated
160   from noise analysis was 14 ± 3.5 pA (**Fig. 3E**), which is close to the estimate for WT-TMC1[6]. Taken
161   together, these findings are consistent with the idea that the G411A mutation influences the
162   mechanical gating but not the unitary conductance of the channel.

163   *Mutations of glycine residues on TM6 shift the activation curves.*

164   We then turned to the glycine residues in TM6. There are two: G518 is close to the extracellular
165   side of the helix, and G539 is closer to the intracellular side (**Fig. 2A-B, Fig. 4A**). From IHCs
166   expressing TMC1-G518A, we obtained maximum currents of 211± 11 pA (n=8) which are
167   comparable to those from WT-TMC1 (**Fig. 4B**, **Supplementary Fig. 3A**). TMC1-G518A activation
168   curves were shifted to the right by ~110 nm (X_0= 493±16 nm) compared to WT-TMC1 (X_0=380 ±
169   32 nm) (**Fig. 4C-D**). From IHCs expressing TMC1-G539A, we also obtained typical maximum
170   currents of 214 pA ± 38 pA (n=14) and the activation curves were shifted rightward by ~140 nm
171   (X_0= 518 ± 30 nm) (**Fig. 4C**). For both TMC1-G518A and TMC1-G539A, the difference in X_0
172   compared to WT-TMC1 is statistically significant, with p<0.05 (**Fig. 4D)**.

173   Importantly, for both these mutations in TM6, the Z values were not significantly different from
174   those for wild-type TMC1 (**Fig. 4D**). A change in X_0 without a change in Z suggests that these
175   mutations in TM6 alter the open probability of the channel without changing the way it is coupled
176   to the mechanical stimulus. Using a simple two-state model (see Methods), these changes in X_0
177   can be interpreted as an increase in the energy of the open state compared to the closed state of
178   ~0.5 k_BT, thus favoring the closed state. Finally, neither TMC1-G518A nor TMC1-G539A showed
179   a significant effect on single channel currents, with 12 ± 2.5 pA for G518A and 14 ± 2.5 pA for
180   G539A (**Fig. 4E**).

181   The glycine at position 518 is highly conserved: 98% of the TMC sequences in our multiple
182   sequence alignment (MSA) show a glycine at this position. However, only 50% of the sequences
183   have a glycine at position 539. A significant portion of the remaining sequences (41%) have an
184   isoleucine or a valine at this position (**Supplementary Table 2**). These sequences include the
185   closely related mouse TMC3, in which the amino acid corresponding to G539 is an isoleucine
186   (**Supplementary Fig. 3B**). We found that the effect of a G539I mutation in TMC1 was similar to
187   that of G539A (**Fig. 4B-D**): IHCs expressing TMC1-G539I showed normal transduction current
188   amplitude of 190 pA ± 14 pA (n=9) and single channel currents (14 ± 3 pA) but a ~100 nm

189   rightward shift in the activation curves (X_0 = 478 ± 25 nm) compared to WT-TMC1 (**Fig. 4C-D**).
190   Again, no significant change was observed in the Z value, implying that this mutation, similar to
191   TMC1-G539A, does not affect the mechanical sensitivity of the channel **(Fig. 4C-D).**

192   TMC3 has a glycine four residues towards the intracellular side of the protein, equivalent to
193   position 544 in TMC1 (**Fig. 2B, Supplementary Fig. 3B**). We wondered whether a glycine
194   anywhere in this region would provide sufficient flexibility, and so re-introduced a glycine at
195   position 544 in TMC1 lacking the glycine at position 539 (TMC1-G539I/A544G). However, we
196   found that a glycine at position 544 did not substitute well for one at position 539, and the
197   activation curve of TMC1-G539I/A544G was not significantly different from TMC1-G539I alone
198   (**Supplementary Fig. 3C-E**).

199   We conclude that mutation of either of the glycine residues at positions 518 and G539 on TM6
200   reduces the resting open probability, as indicated by the rightward shift in X_0, but does not
201   contribute to the mechanical sensitivity of the channel as measured by the slope Z, or to ion
202   permeation. This is consistent with the idea that flexibility of TM6 is important for channel
203   opening.

D528 on TM6 is Critical for Mechanical Sensitivity and Ion Conduction

205   TM6 contains a central and highly conserved aspartate, D528 (**Fig. 2A-B**). *Tmc1* p.D528N is a
206   recessive deafness mutation in mice[26]. The corresponding residue within the Ca^{2+}-activated Cl^-
207   channel TMEM16A is a lysine (K645 in mouse TMEM16A), which has been linked to the voltage,
208   Ca^{2+} and anion dependence of the channel activation [32]. In the structural models for TMC1, D528
209   faces the channel pore[6, 8, 26] and significantly contributes to the negative surface charge (**Fig. 5A,**
210   **Supplementary Fig. 4A**). To investigate whether D528 plays a role in mechanosensitive gating,
211   we made the following mutations: D528A, D528N and D528E.

212   These mutations are also expected to change the surface electrostatics within the pore cavity
213   (**Supplementary Fig. 4A**). Indeed, we had previously found that IHCs expressing TMC1-D528C
214   show significantly reduced transduction currents (~30% relative to WT-TMC1)[6]. The currents
215   were further diminished—irreversibly—with application of MTSET reagents (down to ~2%
216   relative to wild-type), confirming their location within the pore[6].

217   Here, we first mutated D528 to an alanine to assess the effect of removing the aspartate side chain.
218   We obtained average maximum currents of 80 ± 15 pA (n=5), which are significantly smaller than
219   that for other mutations we examined (**Fig. 5B, Supplementary Fig. 5A**). Remarkably, we found
220   a 40% reduction in the slope of the TMC1-D528A activation curve compared to WT-TMC1 (**Fig.**
221   **5C-D**). In addition, the activation curve was shifted to the right by nearly 190 nm (566 ± 70 nm
222   compared to 380 ± 32 nm). This apparent shift in the half-maximum location can be accounted for
223   by the dramatic change in the slope; the resting open probability was not altered.

224   We then mutated D528 to an asparagine (D528N), which is similar to an aspartate in size but lacks
225   the negative charge. The average maximum current was near normal at 148±18 pA, n=9 (**Fig. 5B,**
226   **Supplementary Fig. 5A**). We found that the D528N mutation also reduced the slope of the

227 activation curve compared to WT-TMC1 (**Fig. 5C,D**). Reduction in slope in both D528A and
228 D528N suggest that the aspartate side chain at this position contributes to the mechanical
229 sensitivity of the channel. Furthermore, there was a leftward shift of the activation curve (X_0= 340
230 nm), indicating an increase in the resting open probability of TMC1-D528N (~20%) compared to
231 WT-TMC1 (~6%) (**Fig. 5C**).

232 As D528 is both negatively charged and situated at a central location within the pore, we reasoned
233 that the loss of charge in these mutants would reduce cation permeation. Consistent with another
234 recent study, we found a striking decrease in TMC1-D528N single channel currents: 3.5 ± 0.5 pA
235 compared to 12.5 ± 2.5 pA for WT-TMC1 (**Fig. 5E**) [6, 26, 43]. We therefore mutated D528 to glutamate,
236 expecting that substitution with a negatively charged residue may have milder effects. IHCs
237 expressing TMC1-D528E showed maximum average transduction currents of 332 pA ± 40 pA
238 (n=11). The large single channel current for this mutant (17± 2.1 pA) suggests that the negative
239 charge of the amino acid at this position is indeed critical for attracting cations to the pore and so
240 contributes to high conductance (**Fig. 5E)**. However, the charge is not the sole determinant of
241 D528's contribution to channel activation: We found that the TMC1-D528E mutant had a lower
242 slope than WT-TMC1 (**Fig. 5B-D**), suggesting that the size of the side chain of D528 matters for
243 gating and that the role of D528 in gating is more than providing a negative charge. The fact that
244 there is no glutamate at this position in a significant fraction of all the TMC sequences in the
245 multiple sequence alignment is also consistent with this observation (**Supplementary Table 3**).
246 Whether the amino acid size is changed by one carbon (D-to-E) or the size kept but the charge
247 removed (D-to-N), the mechanical sensitivity is affected.

248 It is possible that the observed effects of D528 mutations may be indirect through a reduction in
249 Ca^{2+} permeation and its effect on the resting open probability. However, a previously
250 characterized deafness mutation, M412K, also leads to a reduction in Ca^{2+} permeation but no
251 change in the mechanical sensitivity of the channel as represented by the slope of the activation
252 curves [5, 6], so it is more likely that D528 is directly involved in channel gating.

253 *Mutations of positively charged residues near D528 do not significantly alter TMC1's mechanical*
254 *sensitivity*

255 A positively charged residue near D528 is R601 on TM8. Evolutionary coupling analysis revealed
256 that D528 on TM6 strongly coevolves with R601[6]. Indeed this is the second strongest coupling out
257 of all possible analyzed pairs. Within a multiple sequence alignment of ~5000 TMC sequences,
258 90% of sequences have an aspartate at the position equivalent to 528. When it is an aspartate, the
259 amino acid at the position equivalent to 601 is positively charged—either an arginine or a
260 lysine. When 528 is not an aspartate (11%), 601 loses charge and is either a phenylalanine (F) or
261 less frequently an isoleucine (I)—amino acids with hydrophobic chains (**Supplementary Table
262 3**).

263 The proximity of D528 on TM6 to R601 on TM8 in the structural models generated by AlphaFold2
264 suggest that they can form a salt bridge (**Fig. 6A, Supplementary Fig. 4B**). Similarly, in the
265 structurally related hyperosmolality-gated OSCA calcium channels, interactions among TM6,

266 TM7 and TM8 have been implicated in the gating of the channels[44]. In the calcium-gated
267 TMEM16A chloride channels, calcium ions bind among acidic residues in TM6, TM7 and TM8 to
268 activate the channels[14]. To assess the influence of the arginine at 601 on TMC1 gating, we mutated
269 R601 in WT-TMC1 as well as in TMC1-D528N. TMC1-R601A yielded very low whole-cell currents
270 (23 ± 8 pA, n=5), while TMC1-D528N/R601F showed currents (166 ± 40 pA, n=5) comparable to
271 WT-TMC1 (**Fig. 6B**, **Supplementary Fig. 5A**). In both WT-TMC1 and TMC1-D528N, mutation of
272 R601 shifted the activation curves rightward, apparently stabilizing the closed state (R601A:
273 X_0=580±25 nm; D528N/R601F: X_0=510±46 nm) (**Fig. 6C-D**). The shift in X_0 is statistically significant
274 for both (**Fig. 6D**). The Z values, representing mechanical sensitivity of the channel, were not
275 affected by these arginine mutations (**Fig. 6D**).

276 Thus removing a positive charge from TM8 that is likely involved in a salt bridge to TM6 changes
277 the instrinsic energy difference between the open and closed states, without changing the
278 efficiency with which the mechanical stimulus is coupled to channel gating. This implies further
279 that the dramatic change in the mechanical sensitivity of the channel following mutation of D528,
280 as measured by the slope, cannot be explained by electrostatic interaction between D528 and R601
281 but is caused by interaction between D528 and other residues.

282 Discussion

283 We previously used cysteine mutagenesis and cysteine modifying reagents to implicate TMC1
284 transmembrane domains 4-7 in the ion permeation pathway opened by mechanical stimulation[6].
285 Other studies involving mutations in these domains, including M412K [5, 45, 46], D569N [27], T416K,
286 W554L and D528N [27], are consistent with this implication, as are detailed molecular dynamic
287 simulations of ion permeation using predicted TMC1 structures [10]. The opening itself, however,
288 is less well understood.

289 In this study, we used viral gene delivery of mutant TMC1 to TMC1/2-null hair cells to study
290 channel gating. To guide mutations, we first turned to machine-learning based, template-free
291 structure prediction programs, including AlphaFold2[21], to refine our previous homology model[6].
292 The newer, ab initio models predicted a fold for TMC1 (**Fig. 1A-D**) very similar to that based on
293 the known structures of the related TMEM16 channels [6,9], adding confidence in the models.
294 Running AlphaFold2 multiple times with different starting conditions suggested structural
295 diversity, with striking differences in the pore region of TMC1. These predicted conformations
296 suggest that TM3 and TM4 together move away from TM6 to open the channel (**Supplementary
297 Movie** 1). Similarly, distancing of TM4 and TM6 enhances permeation in molecular dynamics
298 simulations of the homology models[12].

299 For TMC1, the idea that conformational changes in TM4 and TM6 might bring their more
300 extracellular portions in close contact and close off the permeation pathway is consistent with a
301 gate for the hair-cell transduction channels that is located outside the binding site for charged
302 blockers [47]. Previous experiments demonstrated that M412 and D569 sites, which face the more
303 intracellular part of the pore, are accessible from the extracellular solution only when the

304   transduction channels are open but not when they are closed [6]; they are also consistent with a
305   gate near the outer part of the pore (**Supplementary Fig. 4A**).

306   Interestingly, the open-like conformations predicted by AlphaFold2 show a pore that is, in its
307   narrowest dimension, not larger than about 6 Å in diameter, which is similar to what has been
308   observed in recent molecular dynamics simulation studies[12]. Careful physiology has suggested
309   a larger open pore diameter, close to 12 Å [8, 29]. It may be that the pore can expand further than
310   suggested in these models, or it may be that large permeant ions can extend partially into the
311   lipid as they pass through the pore [6].

312   Based on the predicted structures, we prepared a total of twelve mutations at seven sites in TMC1.
313   We found that mutations of a set of glycines within the TM6 helix led to rightward shifts in the
314   activation curve without a change in slope. These glycine mutations lower the resting open
315   probability of the channel, suggesting that they reduce the energy of the closed state without
316   changing the way that force produced by tip link tension is conveyed to the gate.

317   On the other hand, mutations of the pore-lining residues G411 on TM4 and D528 on TM6 not only
318   shifted the activation curve but also changed its slope. A reduction in the mechanical sensitivity
319   of the transduction channel, as represented by the slope of the activation curve, suggests that the
320   force applied by the tip link is less efficiently coupled to the relative energies of the open and
321   closed states. According to the classical gating-spring model [48], mechanical force is coupled to the
322   channel through an elastic element known as the gating spring, which has not been molecularly
323   identified. In this model, the slope factor Z of the activation curve (also known as the single
324   channel gating force) is defined as:

325   $$Z = \gamma\, k_{Gs} b,$$

326   where γ is the geometric gain between bundle deflection and gating spring extension; k_{Gs} is the
327   gating spring stiffness; and b is the swing of the gate. Compared to mechanically tight hair
328   bundles such as those from bullfrog, bundles in mammalian cochlea are difficult to stimulate with
329   uniform deflection[49, 50]. Uneven contact of hair cells with the stimulus probe results in
330   underestimation of the Z value, by as much as 85% for IHCs[49, 50]. Still, it is possible to compare
331   the Z values from hair cells expressing mutated TMC1 channels and to determine if Z has been
332   altered by the mutations.

333   In the simple biophysical model, a change in Z may be due to a change in the gating spring
334   stiffness or in the swing of the gate. It is difficult to imagine how the mutation of a single residue
335   in TMC1 could reduce the stiffness of the gating spring; whatever it is, the gating spring must be
336   able to stretch many tens of nanometers and the structure of TMC1 is not conducive to such a
337   huge rearrangement. From biophysical studies of bullfrog hair bundles, the gating swing has
338   been estimated as 4 nm or more[51, 52], a distance much larger than the ~0.5 nm movement suggested
339   by structural modeling that may close the outer part of the pore (Fig. 1D). Thus it is likely that a
340   large movement of one part of the channel propagates to the gate region to open the pore itself.

341   Reduction in Z by mutation could also come about in how efficiently the force produced by the
342   large gating movement changes channel open probability.

343   We have explored the possibility that D528 is coupled to the mechanical stimulus via salt-bridge
344   interactions with nearby positive charges with the protein itself. However, we find that mutations
345   of R601 led to rightward shifts in the activation curves without a change in slope. This suggested
346   that the proposed salt bridge between D528 and R601 may be important for stabilizing the closed
347   channel conformation but doesn't seem to play a role in the way the gate is coupled to the
348   mechanical stimulus.

349   A number of proteins together form the mechanotransduction complex[11]. Previous studies have
350   shown that TMC1 is the major pore-forming component of the complex. TMC1 might also be the
351   force-sensing component of the complex, but it is also possible that tip-link tension is conveyed
352   to a distinct force-sensing protein within the complex, and that a conformational change of that
353   protein then promotes opening of the TMC1 pore [53]. The block of gating compliance by pore-
354   blocking compounds suggests that the pore is intimately associated with the conformational
355   change produced by tension [51, 54]. By changing the slope factor Z with single residue mutations
356   in TM4 and TM6, this study specifically implicates TMC1 as part of the molecular sensor of
357   tension. Based on this result, on ab inito structural modeling, and on gating movements in related
358   channels, we propose also that the gating transition in TMC1 involves a separation of TM4 from
359   TM6, to open the permeation pathway.

360   Methods

361   *Structure predictions.* We compared our previously reported homology model for TMC1 [6] with the
362   newly generated and more refined models by the transform-restrained trRosetta[18],
363   RoseTTAFold[19] and AlphaFold2[21]. The template-free predictions with AlphaFold2 were
364   performed in a Colab notebook setting (Google Research). To obtain multiple conformations, we
365   ran the network multiple times with different seeds. We typically investigated the top 10 of the
366   ranked structures. Structures were aligned in and visualized by PyMOL (Version 2.4,
367   Schrödinger). We aligned and clustered the structures using the program Chimera[2]. The
368   permeation pathways were modeled by the software HOLE [28].

369   *Sequence alignment and evolutionary coupling analysis.* Using EVcouplings software[55] (beta version
370   of v0.1.1), which uses the Markov model-based sequence-search tool JackHMMER[56], we obtained
371   a multiple sequence alignment of 5380 sequences. Alignments were built from the Uniref100[57]
372   dataset downloaded on July 24, 2020 using a maximum of 5 JackHMMER iterations. For further
373   processing in the EVcouplings pipeline, we imposed a fragment requirement for each sequence
374   to align to at least 70% of the query length, and analysis was restricted to just residue positions
375   that contained at least 70% non-gaps. We used the top 100 covarying residue pairs (evolutionary
376   coupligns) for further analysis.

377   *AAV virus preparations.* Mutations were introduced to specific locations in the mouse AAV-
378   Tmc1ex1 vector, carrying a cytomegalovirus (CMV) promoter [6]. We generated TMC1 constructs

379 bearing the following amino acid substitutions: G518A, G539A, G539I, G539/A544G, D528A,
380 D528N, D528E, 601A, R601H, R523H, G411A, R601F/D528N, A544G (GenScript, Piscataway NJ,
381 USA). Constructs were screened with SmaI digest to check for inverted terminal repeat (ITR)
382 integrity before packaging into AAV vectors. Viral vectors were packaged with AAV2 ITRs into
383 the AAV9 capsid serotype PHP.B. Virus were generated and purified by the Viral Core at Boston
384 Children's Hospital with genomic titers (measured with hGH primers) between 1×10^{13} and 5×10^{14}
385 gc/ml. Vectors were aliquoted and stored at -80°C.

386 *AAV virus injections.* Neonatal *Tmc1*$^{\Delta/\Delta}$/*Tmc2*$^{\Delta/\Delta}$ C57BL/6 mice[34] typically born ~ E20, were placed
387 with CD1 foster mothers. All animals were housed and bred in the animal facility at Harvard
388 Medical School. Male and female pups were randomly chosen for the study. Prior to injection,
389 mice were anesthetized using hypothermia. A post-auricular incision was made near the left ear
390 and a cotton ball was inserted to spread the tissue. For round window membrane (RWM)
391 injections, an injection needle made from a 1.4 mm glass capillary and pulled to a ~10 μm
392 diameter tip was positioned just above the RWM to confirm that viral suspension was released
393 when the injection was started. Once confirmed, the needle was inserted through the RWM and
394 1.2 μl was injected using a Nanoliter 2000 Injector (World Precision Instruments) at a rate of 65
395 nl/min. Following the procedure, the surgical incision was closed with sutures. The pups were
396 then put on a 37°C heating board to recover and returned to their cages. Usually three animals
397 were injected in a session, and we typically performed three injection sessions per mutation.

398 *Cochlear dissections.* At P4 to P6, pups were euthanized by rapid decapitation, temporal bones
399 were dissected and the membranous labyrinth was isolated under a dissection microscope.
400 Reissner's membrane was peeled back, and the tectorial membrane and stria vascularis were
401 mechanically removed. Organs of Corti were excised and cultured in medium containing DMEM
402 supplemented with 1% FBS, 10 mM HEPES and 0.05 mg/ml carbenicillin at 37°C in 5% CO_2. Organ
403 of Corti cultures were pinned flat beneath a pair of thin glass fibers glued at one end with Sylgard
404 to an 18-mm round glass coverslip. The tissue was placed in culture for 3-7 days before
405 electrophysiological studies.

406 *FM1-43 uptake assays.* Coverslips with adherent cochlear cultures were placed on a glass-
407 bottomed chamber. The culture media was washed away with Leibovitz's L15 medium three
408 times and then incubated with 2 μM FM1-43 in L-15 for 1 minute followed by incubation with 2
409 mM SCAS in L-15 for 3 minutes and washed with L-15 two additional times before imaging.

410 *Confocal imaging.* Imaging was performed on an Olympus FV1000 confocal microscope. FM1-43
411 fluorescence (excitation at 488 nm with ~5-12 % intensity) was measured on mounted cultures
412 with a 60X (1.1-NA) water-immersion objective.

413 *Electrophysiology.* Transduction currents were recorded from IHCs using a Nikon Eclipse FNI
414 microscope with 60X LWI objective and DIC optics and an Axopatch 200B patch clamp with a
415 Digidata 1440 digitizer controlled by pCLAMP 10 software (Molecular Devices). The whole-cell
416 voltage-clamp configuration was used for recordings. Currents were filtered at 5 Hz with a low-
417 pass eight-pole Bessel filter. For hair-bundle stimulation, custom glass probes were made and

418 polished to a diameter of ~4 μm to match the shape of the inner hair cell bundles. The probe was
419 attached to the probe holder with wax and shielded with grounded aluminum foil. The holder
420 was moved by a piezo stack (Physik Instruments) driven by a custom high voltage piezo driver
421 amplifier. Bundles were displaced for 80 ms with 15 step displacements from -175 nm to 1050
422 nm at 88 nm increments. For recordings, 1.5 mm OD R-6 (8350) glass pipettes were pulled with
423 a Narishige PC-10 puller and coated with pre-warmed wax before use. These patch pipettes were
424 filled with an internal solution containing (in mM): 137 CsCl, 5 EGTA, 10 HEPES, 2.5 Na_2-ATP,
425 0.1 $CaCl_2$ and 3.5 $MgCl_2$, and adjusted to pH 7.4 with CsOH, ~290 mmol/kg. The tissues were
426 bathed in external solution containing (in mM): 137 NaCl, 5.8 KCl, 0.7 NaH_2PO_4, 10 HEPES, 1.3
427 $CaCl_2$, 0.9 $MgCl_2$, 5.6 glucose, vitamins and essential amino acids, adjusted to pH 7.4 with NaOH,
428 ~310 mmol/kg. Cells were held at a -80 mV potential and a separate pipet flowed extracellular
429 solution onto their apical surfaces.

430 *Electrophysiology analysis.* Data were analyzed with Clampfit (Molecular Devices) and ORIGIN
431 (OriginLab). The average maximum current amplitudes as a function of probe displacement were
432 plotted for each hair cell and fitted with a Boltzmann equation using ORIGIN as follows:

433
$$Y = \frac{A1 - A2}{1 + \exp\left[\frac{(X - X_0)}{dx}\right]} + A2$$

434 The data were then normalized for each cell, such that A1 and A2 range from 0 to 1 to allow
435 comparison across cells. Z values were derived from the relationship $1/dx = Z/k_BT$. For each TMC1
436 variant, the average X_0 and Z values were calculated as the mean ± SEM of all cells. The number
437 of cells (n) is indicated in the text and figures. Student's t-test was used to compare the means,
438 and p values < 0.05 are marked as significant. For mutations with no significant change in slope,
439 the corresponding change in intrinsic energy difference was estimated as $\Delta X_0/dx$ in units of k_BT.
440 For non-stationary noise analysis, the variance of the responses was plotted against the mean for
441 each cell. As before, we averaged the data within 1 pA intervals [6] and fitted with a parabola to
442 derive the relevant values:

443
$$\sigma^2 = \sigma_0^2 + iI - \frac{I^2}{N}$$

444 where σ2 is the variance, i is the single-channel current, I is the whole-cell current and N is the
445 number of channels[39]. Cells were included in the analysis only if the plot of σ² vs. I yielded a
446 parabolic dataset that was fit well by the equation above. Statistics are based on at least three cells
447 for each condition.

448 **Author contributions:** N.A., B.P, K.D.K. and D.P.C designed the experiments. B.P. acquired
449 electrophysiology data. K.D.K. assembled instrumentation and performed FM1-43 assays and
450 confocal imaging. P.T. performed cochlear dissections. Y.L. bred and maintained mice and
451 performed cochlear injections. K.P.B. and D.S.M mapped evolutionarily coupled residue pairs
452 onto structures. N.A., K.D.K., B.P., and D.P.C wrote the manuscript.

458 **Competing interests:** The authors declare no competing interests.
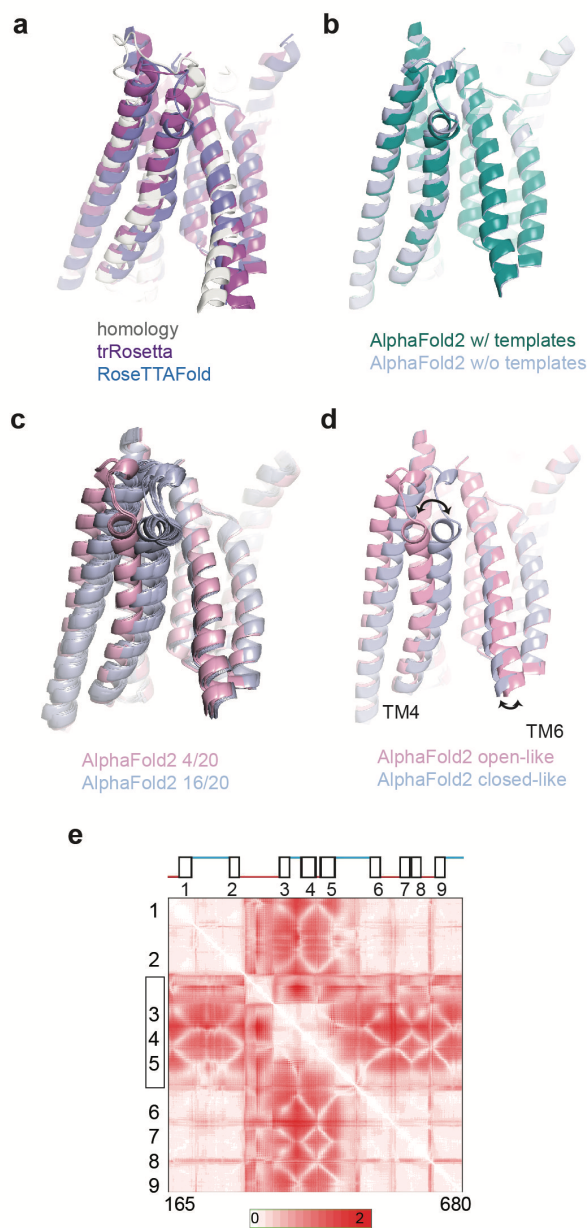
FIGURES

Figure 1. Similarity in TMC1 structural predictions. **a** Structural models for mouse TMC1. Shown in foreground are TMs 3,4,6 and 8, viewed from within the membrane plane. Gray represents an iTasser model based on homology to TMEM16 channels. Purple shows a prediction by trRosetta, not based on other structures. Blue is a predicted model by RoseTTAFold, also not based on known structural templates. The three models are nearly identical. **b** Structural models for TMC1 from AlphaFold2. Green shows a model based on templates such as TMEM16A. Blue is the ab initio model not based on known structures. In the pore region they are the same within 1-2 Å. **c** Two models from AlphaFold2, generated with multiple seed parameters. In 20 model

15

iterations, 16 grouped in one conformation (blue; like that in panel B) and 4 grouped in a different conformation (pink). **d** Representative models from the two groups of conformations in panel C. The conduction pathway for ions is between TM4 and TM6. In the more open conformation (pink), TM4 and TM5 are more distant from TM6 by about 5 Å at the constricted region of the pore. **e** Standard-deviation (SD) maps for all residue-residue (R-R) distances for residues 165-680. For each residue pair, more intense red represents a larger change in distance between the two conformations. TM helices are numbered. The N-terminus, C-terminus and TM10 were not included in the analysis.
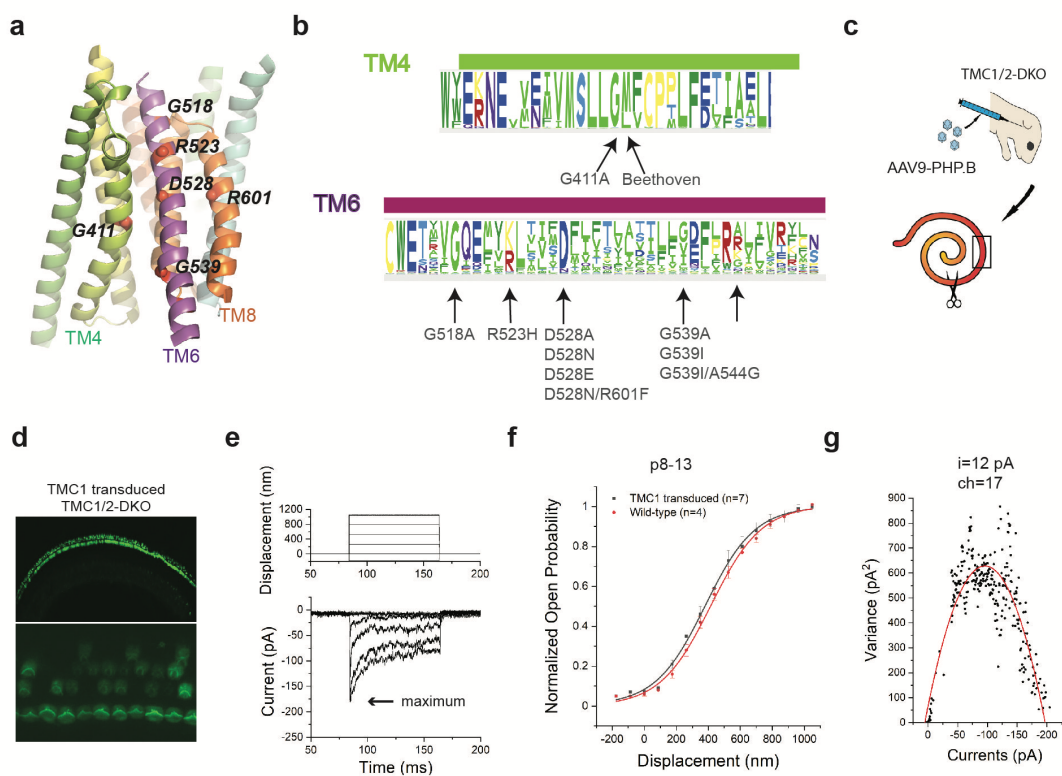
Figure 2. Structure-based mutations of TMC1 and functional assays. a Locations of the mutation sites in a view of the pore region from the plane of the membrane. **b** A sequence logo generated from multiple sequence alignments for TM4 and TM6 regions of TMCs; mutations in this study indicated. **c** Cartoon demonstrating AAV injection of neonatal *Tmc1/2* double-knockout (DKO) animals (top), and separation of the dissected cochlear explants into two sections (bottom). The scissors indicate where the tissue was split. The black box represents the mid-base region, used for electrophysiological recordings of transduction currents. **d** FM1-43 loading of cochlear HCs from *Tmc1/2*-DKO mice expressing virally expressed WT TMC1 channels. The bottom panel is a magnified view at the plane of the bundles. **e** Representative transduction currents in response to -175 to 1050 nm bundle deflections (top panel) recorded from DKO IHCs expressing virally encoded WT-TMC1. **f** Activation curves. Normalized open probability curves are shown as a function of stimulus displacement (nm), in WT-mice and *Tmc1/2*-DKO mice expressing WT-TMC1. The curves are fitted with a Boltzmann equation. **g** Single channel current estimate (i=12 pA) and number of channels (ch=17) based on non-stationary noise analysis from a hair cell expressing viral WT-TMC1. Variance is plotted as a function of current and fitted with a parabolic equation.
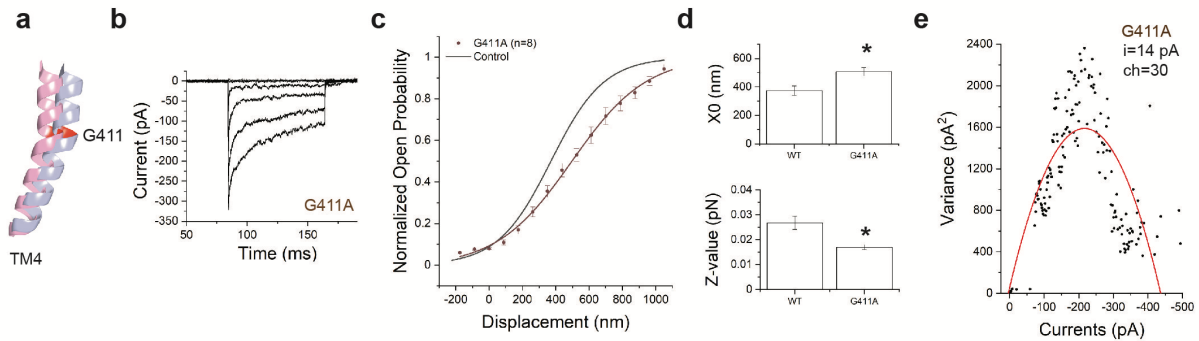
17

Figure 3. Mutation of G411 on TM4 shifts the activation curve and changes the slope. a Representation of TM4 showing G411A mutation site. Pink and blue represent the open- and closed-like configurations, respectively. **b** Representative transduction currents in response to -175 to 1050 nm deflections from IHCs expressing TMC1-G411A. **c** Activation curves from TMC1-G411A (red) and WT-TMC1 (black) expressed in DKO mice. **d** Fitting parameters X_0 (position of half-activation) and Z (slope factor). Significance in differences in X_0 (p=0.01) and Z-values (p=0.01) are indicated stars above the bars. **e** Non-stationary noise analysis for a hair cell expressing TMC1-G411A. Conductance did not change significantly.
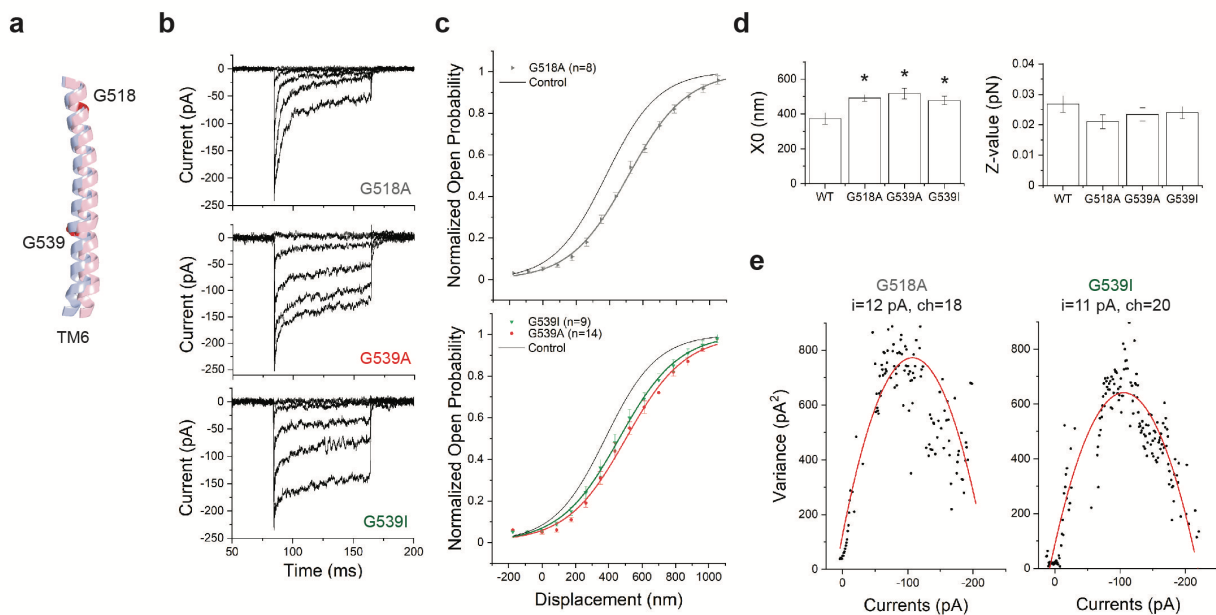
18

Figure 4. Mutation of G518 or G539 on TM6 shifts the activation curves without changing the slope. **a** Relative position of TM6 in open-like (pink) and closed-like (blue) structural models generated by AlphaFold2, showing G518 and G539. The predicted structures were aligned globally. **b** Representative transduction currents in IHCs expressing TMC1-G518A (top), TMC1-G539A (middle) and TMC1-G539I (bottom). **c** Activation curves from TMC1-G518A (top) and TMC1-G539A and TMC1-G539I (bottom). In both, the control WT-TMC1 activation curve is shown in black. **d** Fitting parameters X_0 and Z. All three mutations shifted the activation curves (with p-values = 0.03, 0.01, 0.02) without significantly changing slope (with p-values = 0.08, 0.44, 0.13, respectively). **e** Non-stationary noise analysis for single hair cells expressing G518A (left) or G539I (right). Conductance did not significantly change from wild-type.
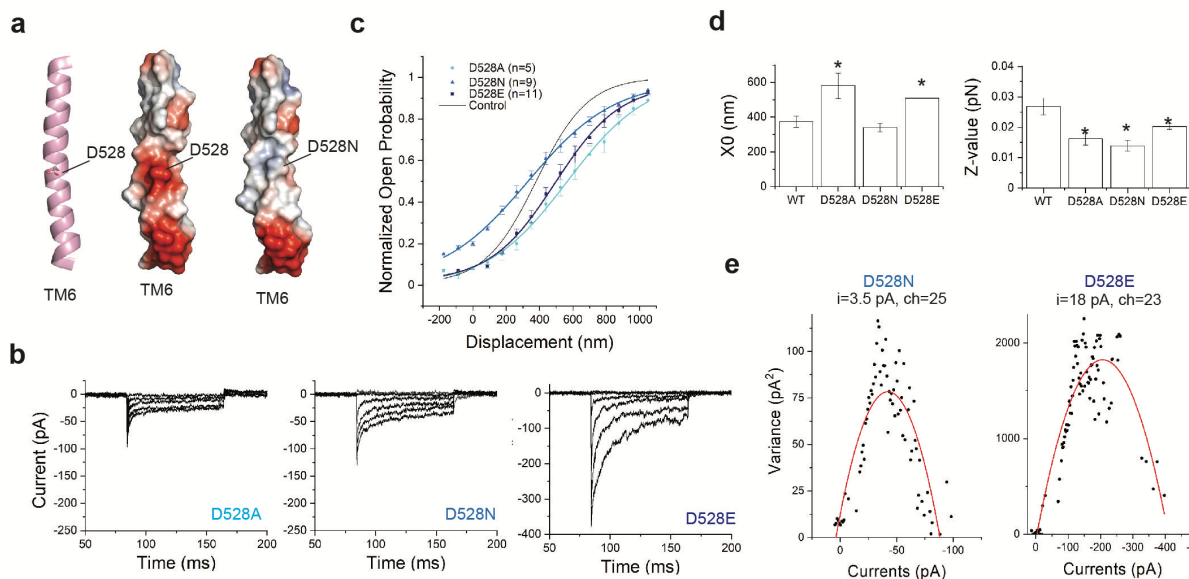
19

Figure 5. Mutations of D528 shift the activation curve and change the slope, and can change single channel currents. a Position of D528 within TM6 of TMC1. TM6 is shown cartoon representation (left panel) with the side-chain of D528 highlighted in stick. The right panels show TM6 in electrostatic surface representation. Electrostatic surface potentials are colored red and blue for negative and positive charges, respectively, and white color represents neutral residues. **b** Transduction currents from TMC1 bearing D528A (left), D528N (middle) or D528E (right) mutations. **c** Activation curves from IHCs expressing TMC1-D528A (cyan), D528N (blue) or D528E (navy). The fit for WT-TMC1 is shown in black as reference. **d** X_0 and Z for each mutation compared to WT. All three mutations reduced the slope (p-values<0.01), whereas the midpoints of curves for D528A and D528E (p-values= 0.01, 0.01), but not D528N (p-value=0.33), were shifted. **e** Non-stationary noise analysis for TMC1-D528N (left) and TMC1-D528E (right). Preservation of charge in the D528E mutant preserved single-channel conductance.
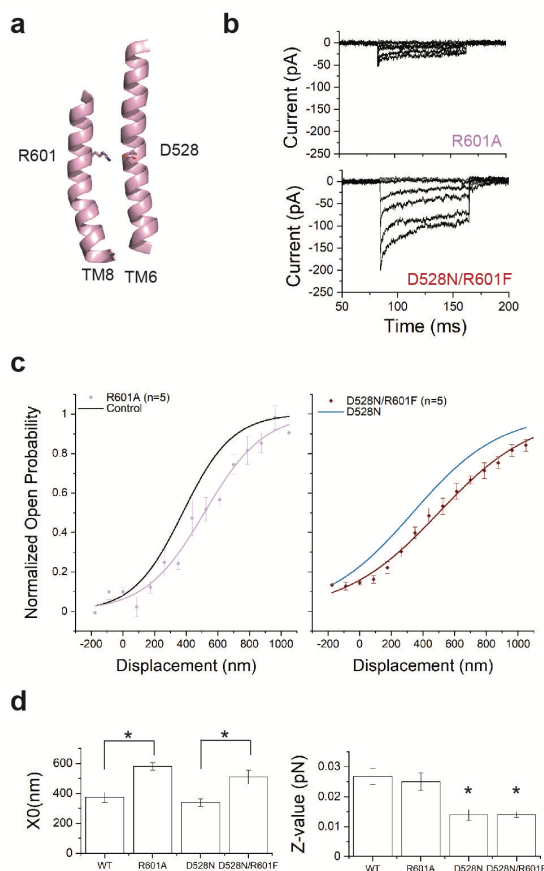
20

Figure 6: Mutation of R601 shifts the activation curve without changing slope. **a** Representation of TM8 showing R601. **b** Transduction currents from TMC1-R601A (top) and TMC1-D528N/R601F mutation (bottom). **c-d** Activation curves from IHCs expressing TMC1-R601A (lilac) or TMC1-D528N/R601F (crimson). The fits for wild-type TMC1 (C, black) and TMC1-D528N (D, blue) are shown as reference. **d** X_0 and Z values. R601A shifts the curve (p-value<0.01) from WT without significantly changing slope (p-value=0.1), and shifts the curve from D528N (p-value<0.01) without further changing slope (p-value=0.3).

21

REFERENCES

1. Corey DP, Hudspeth AJ. Kinetics of the Receptor Current in Bullfrog Saccular Hair Cells. *J Neurosci* **3**, 962-976 (1983).

2. Zhao B, *et al.* Tmie Is an Essential Component of the Mechanotransduction Machinery of Cochlear Hair Cells. *Neuron* **84**, 954-967 (2014).

3. Giese APJ, *et al.* Cib2 Interacts with Tmc1 and Tmc2 and Is Essential for Mechanotransduction in Auditory Hair Cells. *Nat Commun* **8**, 43 (2017).

4. Beurg M, Xiong W, Zhao B, Muller U, Fettiplace R. Subunit Determination of the Conductance of Hair-Cell Mechanotransducer Channels. *Proc Natl Acad Sci U S A* **112**, 1589-1594 (2015).

5. Pan B, *et al.* Tmc1 and Tmc2 Are Components of the Mechanotransduction Channel in Hair Cells of the Mammalian Inner Ear. *Neuron* **79**, 504-515 (2013).

6. Pan B, *et al.* Tmc1 Forms the Pore of Mechanosensory Transduction Channels in Vertebrate Inner Ear Hair Cells. *Neuron* **99**, 736-753 e736 (2018).

7. Medrano-Soto A, Moreno-Hagelsieb G, McLaughlin D, Ye ZS, Hendargo KJ, Saier MH, Jr. Bioinformatic Characterization of the Anoctamin Superfamily of Ca2+-Activated Ion Channels and Lipid Scramblases. *PLoS One* **13**, e0192851 (2018).

8. Ballesteros A, Fenollar-Ferrer C, Swartz KJ. Structural Relationship between the Putative Hair Cell Mechanotransduction Channel Tmc1 and Tmem16 Proteins. *eLife* **7**, (2018).

9. Liang X, *et al.* Cib2 and Cib3 Are Auxiliary Subunits of the Mechanotransduction Channel of Hair Cells. *Neuron* **109**, 2131-2149 e2115 (2021).

10. Kalienkova V, Clerico Mosina V, Paulino C. The Groovy Tmem16 Family: Molecular Mechanisms of Lipid Scrambling and Ion Conduction. *J Mol Biol* **433**, 166941 (2021).

11. Corey DP, Akyuz N, Holt JR. Function and Dysfunction of Tmc Channels in Inner Ear Hair Cells. *Cold Spring Harb Perspect Med* **9**, (2019).

12. Walujkar S, Lotthammer JM, Nisler CR, Sudar JC, Ballesteros A, Sotomayor M. In Silico Electrophysiology of Inner-Ear Mechanotransduction Channel Tmc1 Models. *bioRxiv*, 2021.2009.2017.460860 (2021).

13. Jia Y, *et al.* Tmc1 and Tmc2 Proteins Are Pore-Forming Subunits of Mechanosensitive Ion Channels. *Neuron* **105**, 310-321 e313 (2020).

14. Paulino C, Kalienkova V, Lam AKM, Neldner Y, Dutzler R. Activation Mechanism of the Calcium-Activated Chloride Channel Tmem16a Revealed by Cryo-Em. *Nature* **552**, 421-425 (2017).

15. Falzone ME, *et al.* Structural Basis of Ca(2+)-Dependent Activation and Lipid Transport by a Tmem16 Scramblase. *eLife* **8**, (2019).

16. Lam AKM, Dutzler R. Mechanism of Pore Opening in the Calcium-Activated Chloride Channel Tmem16a. *Nat Commun* **12**, 786 (2021).

17. Khelashvili G, Falzone ME, Cheng X, Lee BC, Accardi A, Weinstein H. Dynamic Modulation of the Lipid Translocation Groove Generates a Conductive Ion Channel in Ca(2+)-Bound Nhtmem16. *Nat Commun* **10**, 4972 (2019).

18. Yang H, *et al.* An Improved Method for Estimating Antibody Titers in Microneutralization Assay Using Green Fluorescent Protein. *J Biopharm Stat* **26**, 409-420 (2016).

19. Baek M, *et al.* Accurate Prediction of Protein Structures and Interactions Using a Three-Track Neural Network. *Science*, (2021).

20. Rohl CA, Strauss CE, Misura KM, Baker D. Protein Structure Prediction Using Rosetta. *Methods Enzymol* **383**, 66-93 (2004).

21. Jumper J, *et al.* Highly Accurate Protein Structure Prediction with Alphafold. *Nature*, (2021).

22. Moult JF, K., Kryshtafovych A, Schwede T, Topf M. Critical Assessment of Techniques for Protein Structure Prediction, Fourteenth Round.).

23. Corey DP, Hudspeth AJ. Ionic Basis of the Receptor Potential in a Vertebrate Hair Cell. *Nature* **281**, 675-677 (1979).

24. Kros CJ, Rusch A, Richardson GP. Mechano-Electrical Transducer Currents in Hair Cells of the Cultured Neonatal Mouse Cochlea. *Proc Biol Sci* **249**, 185-193 (1992).

25. Ricci AJ, Fettiplace R. Calcium Permeation of the Turtle Hair Cell Mechanotransducer Channel and Its Relation to the Composition of Endolymph. *J Physiol* **506 (Pt 1)**, 159-173 (1998).

26. Beurg M, *et al.* New Tmc1 Deafness Mutations Impact Mechanotransduction in Auditory Hair Cells. *J Neurosci* **41**, 4378-4391 (2021).

27. Beurg M, Barlow A, Furness DN, Fettiplace R. A Tmc1 Mutation Reduces Calcium Permeability and Expression of Mechanoelectrical Transduction Channels in Cochlear Hair Cells. *Proc Natl Acad Sci U S A* **116**, 20743-20749 (2019).

28. Smart OS, Neduvelil JG, Wang X, Wallace BA, Sansom MS. Hole: A Program for the Analysis of the Pore Dimensions of Ion Channel Structural Models. *J Mol Graph* **14**, 354-360, 376 (1996).

29. Farris HE, LeBlanc CL, Goswami J, Ricci AJ. Probing the Pore of the Auditory Hair Cell Mechanotransducer Channel in Turtle. *J Physiol* **558**, 769-792 (2004).

30. Chen JE, Huang CC, Ferrin TE. Rrdistmaps: A Ucsf Chimera Tool for Viewing and Comparing Protein Distance Maps. *Bioinformatics* **31**, 1484-1486 (2015).

31. Hopf TA, *et al.* Sequence Co-Evolution Gives 3d Contacts and Structures of Protein Complexes. *eLife* **3**, (2014).

32. Peters CJ, *et al.* The Sixth Transmembrane Segment Is a Major Gating Component of the Tmem16a Calcium-Activated Chloride Channel. *Neuron* **97**, 1063-1077 e1064 (2018).

33. Paulino C, *et al.* Structural Basis for Anion Conduction in the Calcium-Activated Chloride Channel Tmem16a. *eLife* **6**, (2017).

34. Kawashima Y, *et al.* Mechanotransduction in Mouse Inner Ear Hair Cells Requires Transmembrane Channel-Like Genes. *J Clin Invest* **121**, 4796-4809 (2011).

35. Askew C, *et al.* Tmc Gene Therapy Restores Auditory Function in Deaf Mice. *Sci Transl Med* **7**, 295ra108 (2015).

36. Lee J, *et al.* Efficient Viral Transduction in Mouse Inner Ear Hair Cells with Utricle Injection and Aav9-Php.B. *Hear Res* **394**, 107882 (2020).

37. Ivanchenko MV, *et al.* Preclinical Testing of Aav9-Php.B for Transgene Expression in the Non-Human Primate Cochlea. *Hear Res* **394**, 107930 (2020).

38. Hudspeth AJ, Choe Y, Mehta AD, Martin P. Putting Ion Channels to Work: Mechanoelectrical Transduction, Adaptation, and Amplification by Hair Cells. *Proc Natl Acad Sci U S A* **97**, 11765-11772 (2000).

39. Sigworth FJ. The Variance of Sodium Current Fluctuations at the Node of Ranvier. *J Physiol* **307**, 97-129 (1980).

40. Holton T, Hudspeth AJ. The Transduction Channel of Hair Cells from the Bull-Frog Characterized by Noise Analysis. *J Physiol* **375**, 195-227 (1986).

41. Ding S, Ingleby L, Ahern CA, Horn R. Investigating the Putative Glycine Hinge in Shaker Potassium Channel. *J Gen Physiol* **126**, 213-226 (2005).

42. Luque I, Mayorga OL, Freire E. Structure-Based Thermodynamic Scale of Alpha-Helix Propensities in Amino Acids. *Biochemistry* **35**, 13681-13688 (1996).

43. Beurg M, Nam JH, Fettiplace R. The Speed of the Hair Cell Mechanotransducer Channel Revealed by Fluctuation Analysis. *J Gen Physiol* **153**, (2021).

44. Jojoa-Cruz S, *et al.* Cryo-Em Structure of the Mechanically Activated Ion Channel Osca1.2. *eLife* **7**, (2018).

45. Beurg M, Goldring AC, Fettiplace R. The Effects of Tmc1 Beethoven Mutation on Mechanotransducer Channel Function in Cochlear Hair Cells. *The Journal of general physiology* **146**, 233-243 (2015).

46. Corns LF, Johnson SL, Kros CJ, Marcotti W. Tmc1 Point Mutation Affects Ca2+ Sensitivity and Block by Dihydrostreptomycin of the Mechanoelectrical Transducer Current of Mouse Outer Hair Cells. *J Neurosci* **36**, 336-349 (2016).

47. Marcotti W, van Netten SM, Kros CJ. The Aminoglycoside Antibiotic Dihydrostreptomycin Rapidly Enters Mouse Outer Hair Cells through the Mechano-Electrical Transducer Channels. *J Physiol* **567**, 505-521 (2005).

48. Markin VS, Hudspeth AJ. Gating-Spring Models of Mechanoelectrical Transduction by Hair Cells of the Internal Ear. *Annu Rev Biophys Biomol Struct* **24**, 59-83 (1995).

49.   Nam JH, Peng AW, Ricci AJ. Underestimated Sensitivity of Mammalian Cochlear Hair Cells Due to Splay between Stereociliary Columns. *Biophysical journal* **108**, 2633-2647 (2015).

50.   Karavitaki KD, Corey DP. Sliding Adhesion Confers Coherent Motion to Hair Cell Stereocilia and Parallel Gating to Transduction Channels. *J Neurosci* **30**, 9051-9063 (2010).

51.   Howard J, Hudspeth AJ. Compliance of the Hair Bundle Associated with Gating of Mechanoelectrical Transduction Channels in the Bullfrog's Saccular Hair Cell. *Neuron* **1**, 189-199 (1988).

52.   Cheung EL, Corey DP. Ca2+ Changes the Force Sensitivity of the Hair-Cell Transduction Channel. *Biophysical journal* **90**, 124-139 (2006).

53.   Christensen AP, Corey DP. Trp Channels in Mechanosensation: Direct or Indirect Activation? *Nat Rev Neurosci* **8**, 510-521 (2007).

54.   Martin P, Bozovic D, Choe Y, Hudspeth AJ. Spontaneous Oscillation by Hair Bundles of the Bullfrog's Sacculus. *J Neurosci* **23**, 4533-4548 (2003).

55.   Marks DS, *et al.* Protein 3d Structure Computed from Evolutionary Sequence Variation. *PLoS One* **6**, e28766 (2011).

56.   Johnson LS, Eddy SR, Portugaly E. Hidden Markov Model Speed Heuristic and Iterative Hmm Search Procedure. *BMC Bioinformatics* **11**, 431 (2010).

57.   Suzek BE, Wang Y, Huang H, McGarvey PB, Wu CH, UniProt C. Uniref Clusters: A Comprehensive and Scalable Alternative for Improving Sequence Similarity Searches. *Bioinformatics* **31**, 926-932 (2015).